Impact of frequent assimilation of surface and satellite observations in an MCS case during RELAMPAGO field campaign. Part I: impact on the analysis

Paola Belén Corrales[*,a,b,c], Victoria Galligani[a,b,c], Juan Ruiz[a,b,c], Luiz Sapucci[f], María Eugenia Dillon[d,e], Yanina García Skabar[d,e,c], Maximiliano Sacco[d]

[a] *Universidad de Buenos Aires, Facultad de Ciencias Exactas y Naturales, Departamento de Ciencias de la Atmósfera y los Océanos. Buenos Aires, Argentina.*
[b] *CONICET – Universidad de Buenos Aires. Centro de Investigaciones del Mar y la Atmósfera (CIMA). Buenos Aires, Argentina.*
[c] *CNRS – IRD – CONICET – UBA. Instituto Franco-Argentino para el Estudio del Clima y sus Impactos (IRL 3351 IFAECI). Buenos Aires, Argentina.*
[d] *Servicio Meteorológico Nacional de Argentina*
[e] *CONICET (Consejo Nacional de Investigaciones Científicas y Técnicas)*
[f] *National Institute for Space Research, Brazil, Center for Weather Forecasting and Climate Studies*

Abstract

The impact of assimilating high-resolution surface networks and satellite observations using the WRF-GSI-LETKF is evaluated. We conducted a case study corresponding to a huge mesoscale convective system (MCS) developed over central and north-eastern Argentina during November, 22th, 2018. The accumulated precipitation observed during the transit of the MCS was quite high with values over 200 mm over the northern part of the domain. This MCS developed during the Intense Observing Period (IOP) of the RELAMPAGO field campaign during Nov. 2018.

We used the GSI-4DLETKF to produce analyses assimilating observations every hour with 10-km horizontal grid spacing and a 60-members ensemble initialized from the deterministic GFS run adding random perturbations with climatological covariance. A multiphysics approach is also used to represent model errors, using different physics configurations (a combination of PBL and convection parameterizations). We conducted four assimilation experiments using different sets of observations: CONV with conventional observations from prepBUFR, AUT that uses CONV observations plus automatic station networks, SATWND add satellite-derived winds and RAD includes satellite radiances from AMSU, HIRS, MHS, ATMS, AIRS and IASI. We found that the assimilation of observations with high temporal and spatial frequency generate an important impact on the PBL, primarily on the precipitable water content, that leads to the development of deep convection and heavy precipitation closer to the observed case study. The assimilation of radiance observations produces a better development of the convection mainly during the mature state of the MCS leading to an increase in the accumulated precipitation.

Key words: Regional Data Assimilation, Surface Obsevations, Satellite Observations

1. Introduction

Severe weather events cause significant human and material losses around the world. A large number of these phenomena are associated with the occurrence of deep moist convection including tornadoes, intense wind gusts, extreme precipitation in short time periods, large hail, and lightning. Southern South America has been shown to have the highest frequency of favorable conditions for high-impact meteorological events (Brooks et al., 2003) and the highest occurrence of large hail events (Cecil and Blankenship, 2012). This is also confirmed by observational evidence and high impact weather reports (Matsudo et al., 2015; Rasmussen et al., 2014).

Forecasting mesoscale meteorological phenomena and particularly deep moist convection is a scientific and technological challenge due to several factors. On the one hand, mesoscale phenomena have limited predictability, while on the other hand, there is great difficulty in diagnosing the state of the atmosphere at small spatial and short temporal scales (for example from 1 to 10 kilometers and in the order of minutes). To solve this problem, data assimilation (DA) at the mesoscale is a topic that has gained increasing interest since it can provide appropriate initial conditions for the initialization of high-resolution forecasts (Sun et al., 2014).

DA methods can successfully be implemented by using observations with sufficient temporal and spatial resolution to characterize mesoscale atmospheric circulations. However surface observations, which directly measure the atmospheric state, have limited availability in South America. Other types of observations are being assimilated with relatively high spatial and temporal resolution, such as satellite radiance observations or retrieval products. Radiance observations particularly, are indirect measurements and are more difficult to incorporate to DA systems as they require complex forward models.

---
[*]Corresponding Author
Email address: `paola.corrales@cima.fcen.uba.ar` (Paola Belén Corrales)

The assimilation of conventional observations from surface stations have an important role at improving the initial conditions that lead to better forecasts. For example, Ha and Snyder (2014) showed that the assimilation of temperature and dew point temperature systematically improved the structure of the simulated planetary boundary layer that subsequently resulted in a better precipitation forecast over the U.S.

Given the sparsity of the local conventional observing network it is important to explore the potential benefits of including additional sources of observations at a regional scale. Recently Zhu et al. (2019) studied the impact of assimilating satellite radiance data within a frequently updated regional system and showed a positive improvement for all variables, in particular for relative humidity at upper levels. Previous work has shown a positive impact at incorporating temperature and humidity profiles derived from the multispectral infrared sensors (i.e. AIRS and IASI) in a regional domain application. Miyoshi and Kunii (2012) assimilated observations, atmospheric temperature and humidity profile data from the AIRS and found improvement on the tracking of two typhoons. Dillon et al. (2019) also assimilated retrievals from the AIRS sensor and reported improvements on the thermodynamic variables and the regional circulation. Moreover Bao et al. (2015) studied the impact on temperature and humidity forecast over western USA while assimilating microwave and infrared radiance data and found a reduction in the temperature bias at low and mid-levels as a result of the microwave observations but an opposite effect for infrared data. Satellite-derived winds from water vapor channels and cloud drift motion vectors also have an overall positive impact on analysis and short-range forecasts (Gao et al., 2015).

Having analyses with higher temporal resolution than those available from global forecasting systems (e.g. at hourly or sub-hourly) and using an increased number of regional observations that are not assimilated in global DA systems are some of the advantages of regional DA. Previous work has shown promising results on mesoscale DA in the region using different approaches such as LETKF; (Dillon et al., n.d., 2016) and 3D-Var (gustavo Goncalves de Goncalves et al., 2015). In particular, the use of ensemble-based methods have shown great potential for data assimilation in these scales, as they are able to characterize the flow-dependent evolution of the background error covariances. Moreover, the use of ensembles also provides valuable information about the uncertainties in the forecast. Recently a rapid-refresh ensemble-based DA system has been experimentally implemented during the Remote sensing of Electrification, Lightning, And Mesoscale/microscale Processes with Adaptive Ground Observations (RELAMPAGO) Field Campaign (central Argentina, November-December 2018, Nesbitt et al. (2021)) with promising results (Dillon et al., n.d.). This system assimilated data from high-resolution surface networks, AMDAR data from local aircraft flights, soundings, AIRS retrievals, high-resolution GOES-16 wind estimates, and local radar data every hour with a grid spacing of 10 km. The forecast initialized from the analyses shows an overall similar performance to cold-start initializations from the Global Forecast System analysis, and even a positive impact in some cases.

One important challenge of regional data assimilation systems is the assessment of their representation of the true atmospheric state and the skill of the forecasts initialized using their analysis as initial conditions. In this sense, the observations and measurements taken during the intense observing period of RELAMPAGO are an invaluable resource to validate a regional data assimilation system.

The main objectives of this work are: to evaluate the impact of different observation types, including frequent surface observations, satellite-derived winds and clear-sky satellite radiances from different platforms, into a regional frequent-update ensemble-based data assimilation system. The experiments are conducted using the Local Ensemble Transform Kalman filter implemented within the GSI-WRF data assimilation system. The evaluation is performed using a case study approach involving a gigantic Mesoscale Convective System (MCS) developed over Southern South America during 22-23 November 2018 during the intense observation period (IOP) of the RELAMPAGO field campaign. On 22 November a cold front crossed the center of Argentina triggering isolated convective cells that rapidly grew upscale into an exceptionally large MCS. The MCS traveled approximately 2500 km from south to north, dissipating over Paraguay and Southern Brazil after 42 hours. To the north of the region, a warm front contributed to the development of isolated multicells that ultimately grew and merged with the MSC. The paper is organized as follows. The data assimilation system, the experimental design and observations used is presented in section 2. Results are discussed in section 3 and finally, conclusions are summarized in section 4.

2. Data and Methods

The model simulations for the case study were performed using the version 3.9.1 of the non-hydrostatic Advanced Research version of the Weather Research and Forecasting (WRF-ARW (V3.9), Skamarock et al. (2018)) model. The resolution was 10 km (150 x 200 grid points) on the horizontal and 37 levels on the vertical with the top of the atmosphere at 50 hPa. The initial and boundary conditions are provided by the Global Forecasting System (GFS) analysis (0.25° horizontal resolution and 6 hour temporal resolution, (**???**)). The domain covers the area indicated in Figure 1 to capture the development of the MCS during the simulated period.

The analyses are generated using the Local Ensemble Transform Kalman Filter (LETKF) implementation (V1.3, Hunt et al. (2007)) part of the Gridpoint Statistical Interpolation analysis system (GSI V3.8; Hu et al. (2018)). A rapid update cycle approach is implemented with hourly analysis and a centered assimilation window, meaning that all the observations within ± 30 minutes of the analysis

2

time are assimilated. Observations are assimilated in a 4D approach by comparing them with the corresponding first guess state at 10-minute intervals. For radiance observations, the Community Radiative Transfer Model version 2.3 (CRTM; Han et al. (2006)) was used as an observation operator to calculate model-simulated brightness temperatures.

To reduce the effect of spurious correlations in the estimation of error covariances, we use a horizontal localization radius of 180 km and a vertical localization radius of 0.4 (in log pressure coordinates) as in Dillon et al. (n.d.) for all types of observations. A relaxation-to-prior inflation (Whitaker and Hamill, 2012) is applied with an inflation parameter $\alpha = 0.9$ to mitigate the impact of sampling errors and to consider model errors not accounted for by the multi-model ensemble approach.

We use a 60-member ensemble where the ensemble mean at the beginning of the data assimilation cycle is initialized using the GFS deterministic analysis. Since the publicly available GFS ensemble members change at each cycle **(alguna fuente)** we used random perturbations to generate the initial ensemble perturbations. This method also helps to prevent an underestimation of the ensemble spread (Ouaraini et al., 2015). The perturbations are generated as scaled differences between two random atmospheric states obtained from the Climate Forecast System Reanalysis (CFSR) data with 0.5° horizontal grid spacing with a smooth time evolution as in (Maldonado et al., 2021; Necker et al., 2020). In this way, we preserved the nearly hydrostatic and geostrophic equilibrium of larger scales. These random perturbations are also applied at the boundaries in order to keep the ensemble spread within the domain.

In addition to random perturbations at the lateral boundaries, a multi-physics scheme is used to better represent the uncertainty in model formulation within the DA system. We use 9 different model configurations consisting on the combination of 3 moist convection schemes (Kain–Fritsch (Kain, 2004), Grell–Freitas (Grell and Freitas, 2013), and Betts–Miller–Janjić (Janjić, 1994)) and 3 planetary boundary layer schemes (Yonsei University Scheme (Hong, Noh, et al., 2006), Mellor–Yamada–Janjic Scheme (Janjić, 1994), and Mellor–Yamada Nakanishi Niino (Nakanishi and Niino, 2009)). All ensemble members used the same land-surface model (Noah-MP, Chen and Dudhia (2001)) and microphysics (WRF single-moment 6–class squeme (Hong, Kim, et al., 2006)), and radiation processes (RRTMG shortwave and longwave scheme (Iacono et al., 2008)) parameterizations.

2.1. Observations

2.1.1. Conventional and Satellite-derived wind

The conventional and satellite-derived wind observations used are part of the Global Data Assimilation System (GDAS) [**ver cita**]. We assimilated conventional observations included in the Binary Universal Form for Representation of Meteorological Data (PREPBUFR) files generated
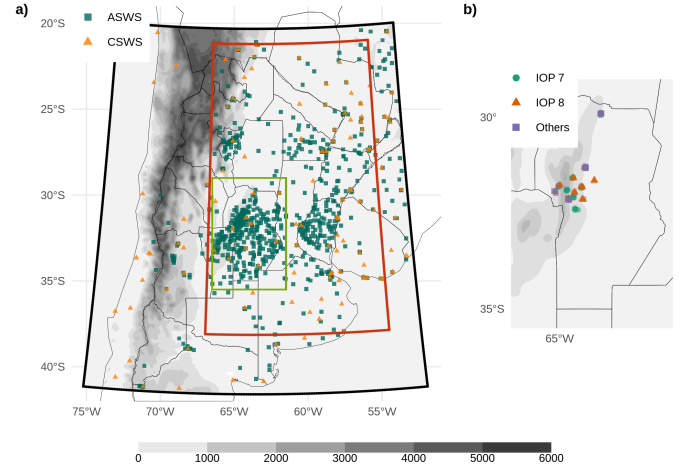

Figure 1: a) The horizontal domain used on the simulations (black box), the inner domain used for the experiment comparison (red box), the region shown in b) (green box) and the locations of Automatic Surface Weather Stations (ASWS, green squares) and Conventional Surface Weather Stations (CSWS, orange triangles). b) Locations of radiosonde launches during the experiment, green dots corresponds to radiosondes launched during IOP 7, orange triangles are radiosondes launched during IOP 8 and purple square are radiosondes launched outside the IOPs. The topography in meters is also shown (filled contours).

at NCEP that consist of surface observations from conventional surface weather stations (CSWS) and ships and upper-air observations from radiosondes and aircrafts. The orange triangles in Figure 1a, are the surface stations and ship locations included in this experiment. The frequency of these observations varied between 1 hour for surface stations and 12/24 hours for most radiosondes in the region.

Satellite-derived wind observations also come from GDAS and includes information from GOES-16 (estimated from the visible, infrared and water vapour channels) and METEOSAT 8 and 11 (visible and water vapour channels). Due to the domain covered by each of these satellites, GOES-16 is the primary source of this type of observation (99 % of observation).

We used additional conventional observations from 866 Automatic Surface Weather Stations (ASWS) that are part of various public and private automatic station networks over Southern South America and are part of RELAMPAGO Data Set repository (Garcia et al., 2019). These stations are indicated as green squares in Figure 1a. They have higher spatial coverage than the CSWS and a sampling frequency of 10 minutes in most cases. The variables measured by the stations varied between networks; all stations measure temperature, but only 395 stations provide humidity, 422 provide pressure and 605 provide wind information.

Table 1 lists all the observation types (i.e., pressure, temperature, specific humidity and wind) available for each source, together with their associated errors. The observation errors were specified following the GSI default config-

Table 1: Observation errors and gross check thresholds for different observation platforms and types.

Code	Platform	Variable	Error	Gross check
CSWS ASWS	Surface weather stations	Pressure	1-1.6 hPa^{*}	3.6 hPa
		Temperature	1.5 K	7 K
		Specific humidity	20 %	8 gKg^{-1}
		Wind	2.2 ms^{-1}	6 ms^{-1}
ADPUPA	Radiosondes	Pressure	1.1-1.2 hPa^{**}	4 hPa
		Temperature	0.8-1.5 K^{*}	8 K
		Specific humidity	20 %	8 gKg^{-1}
		Wind	1.4-3 ms^{-1*}	8 ms^{-1}
AIRCFT	Aircrafts	Temperature	1.47-2.5 K^{+}	7 K
		Wind	2.4-3.6 ms^{-1+}	6.5-7.5 ms^{-1+}
ASCATW	Advance Scatterometers	Wind	1.5 ms^{-1}	5 ms^{-1}
SFCSHP	Ships and Buoys	Pressure	1.3 hPa	4 hPa
		Temperature	2.5 K	7 K
		Specific humidity	20 %	8 gKg^{-1}
		Wind	2.5 ms^{-1}	5 ms^{-1}
SATWND	Satellite-derived winds	Wind	3.8-8 ms^{-1*+}	1.3-2.5 ms^{-1+}

[*] Observation error varied with height
[**] Observations over 600 hPa are rejected
[+] Observation error depends on the report type

uration. In some cases, the error varies with height and it depends on the specific platform (aircraft and satellite-derived wind). In terms of quality control, a gross check was performed by the observation operator by comparing the innovation (the difference between the observation and model-simulated observation based on the first-guess) with a predefined threshold (also included in Table 1).

2.1.2. Satellite radiances

Satellite radiances available through the GDAS data stream, consisting of infrared and microwave observations are used in this study. This includes the Advanced Microwave Sounding Unit - A (AMSU-A), Advanced Technology Microwave Sounder (ATMS), Microwave Humidity Sounder (MHS), High-resolution Infrared Radiation Sounder (HIRS/4), and 2 multispectral sensors, Atmospheric Infrared Sounder (AIRS) and Infrared Atmospheric Sounding Interferometer (IASI) over several satellite platforms (see Table 2). Since the regional domain is located in the mid-latitudes and all satellite platforms are on polar orbits, each sensor scans the area only twice a day with a spatial coverage depending on the satellite swath. For this reason, the number of satellite observations varied significantly among cycles. This is evident in Figure 3a which shows the number of radiance observations assimilated at each analysis cycle as a function of pressure. In particular, the multispectral sensors provided between 100 and 10.000 observations for every scan every 12 hours, contributing 82 % of the total amount of assimilated radiances in our experiments. The vertical location of each radiance ob-

servation was estimated as the model level at which its weighting function was maximized as calculated by CRTM. The multispectral sensors have a good vertical coverage and are able to sense from the lower troposphere and up to the lower stratosphere. The channels whose maximum weighting function is located in the stratosphere were rejected due to the low model top model (50 hPa) used in the experiments.

The channels accepted for assimilation and their associated error were defined using the default GSI configuration. The data preprocessing, which is an essential step in the assimilation of radiances, was performed within the GSI system for each sensor specifically. Firstly a spatial data thinning is applied using a 60 km grid following (Jones et al., 2013; Lin et al., 2017; Singh et al., 2016), where the observations to be assimilated are chosen based on their distance to the model grid points, no the observation quality (based on available data quality predictors) and on the number of available channels (from the same pixel and sensor) that passed the quality control. Also, observations over the sea are preferred from those over land or snow (Hu et al., 2018).

The thinned observations were then bias corrected. The bias correction (BC) has an air-mass dependent and an angle-dependent component (Zhu et al., 2014) and it is calculated as a multi-linear function of N predictors $p_i(x)$, with associated coefficients β_i. Then, the bias corrected brightness temperature can be obtained as:

$$BT_b c = BT + \sum i = 0 N \beta_i p_i(x)$$

GSI has a constant offset bias correction term ($p_0 = 1$). The following predictors are the cloud liquid water content (CLW), the temperature lapse rate at the pressure of maximum weight, the square of the temperature lapse rate at the pressure of maximum weight, and the emissivity sensitivity. Scan angle-dependent bias is modelled as a 4th-order polynomial (Zhu et al., 2014).

The β_i coefficients are usually trained to achieve the best fit between the simulation and the observations. In the GSI system these coefficients are trained using a variational estimation method which solves for the β_i that provides the best fit between the simulation and the observations. The coefficients initialized from the 18 UTC Nov, 11 2018 GFS coefficients were trained during one week of continuous assimilation using the same setup as in the experiments described in the next section. Moreover, the assimilation system was configured to use a constant background error variance of 0.01 to avoid large adjustments in the estimated coefficients at each cycle.

In our experiments, only clear-sky observations are used. For microwave radiances, observations potentially contaminated by clouds are detected using the scattering and Liquid Water Path (LWP) indexes(Weston et al., 2019; Zhu et al., 2016). For the infrared channels cloud contaminated observations are detected using the transmittance profile calculated within the CRTM algorithms. Addition-

Table 2: List of the available sensors in several platforms, the number of accepted channels and the percentage of assimilated observations calculated over all radiance observations.

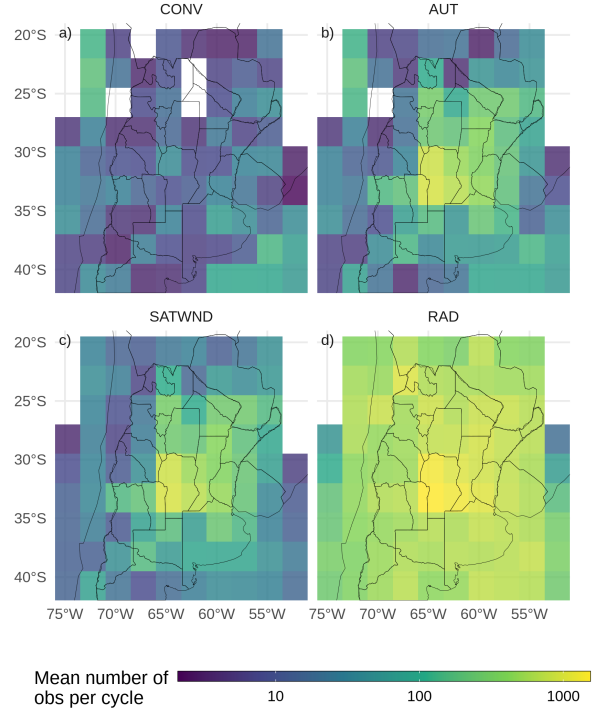| Sensor	Plataform	Assimilated channels	Percentage over total
AIRS	AQUA	118	39.37 %
AMSUA	AQUA	7	1.13 %
	N19	13	1.55 %
	N15	13	3.93 %
	N18	13	3.17 %
	METOP-A	13	1.3 %
ATMS	N20	21	1.16 %
	NPP	21	0.86 %
HIRS4	N19	14	1.79 %
	METOP-A	14	1.37 %
IASI	METOP-A	174	40.07 %
	METOP-B	174	2.94 %
MHS	N19	5	0.44 %
	METOP-A	5	0.46 %
	METOP-B	5	0.44 %

Figure 2: Horizontal spatial distribution of the mean available observations per analysis cycle for the a) CONV, b) AUT c) SATWND and d) RAD experiments calculate over 2.5° boxes.

ally, the GSI quality control for infrared sensors looks for observations over water with a large zenithal angle (over 60°) to reject channels near the visible range that can be contaminated with reflection. It also performs an emissivity check for observations over land for both infrared and microwave radiances.

2.1.3. Validation dataset

To evaluate the performance of the ensemble based data assimilation system presented in this article, we use the following observations datasets:

- The Multi-Network Composite Highest Resolution Radiosonde Data (Earth Observing Laboratory, 2020) from the RELAMPAGO field campaign database consisting of high resolution radiosondes launched from several locations during the Intensive Observation Periods (IOP) along with the operational measurements. Only the measurements/soundings that did not enter the assimilation system were used for validation. The experiment period covers IOP missions 7 and 8 during which 74 radiosondes were launched in a small area near the center of the experimental domain (Figure 1b.

- The Satellite precipitation estimation IMERG Final Run with 0.01° spatial resolution and 30 minutes temporal resolution (Huffman et al., 2018) was used as a reference state to validate the skill 1-hour forecasts to represent the precipitation over the domain.

- Radar observations are used to perform a qualitative and visual assessment of the convection features. The data comes from 9 radars located on the domain and

is provided by the Argentine C-band Doppler dual-polarization weather radar network (de Elía et al., 2017) with a temporal frequency of 10 minutes. For this work only the maximum reflectivity in the column (COLMAX) field closest to the analysis time was used.

2.2. Experimental design

To investigate the impact of different observations upon the analysis, four data assimilation experiments were performed using different observation sets (Table 3). The CONV experiment uses only convectional observations from PREPBUFR. In a second experiment, referred to as AUT, we assimilate all the observations included in CONV plus the 10-minute frequency surface observations from ASWS. In the third experiment, referred to as SATWND, we assimilate all the observations of the AUT experiment and the satellite-derived motion winds. Finally, a fourth experiment referred to as RAD assimilates all available clear-sky observations from sensors onboard polar orbit satellites as described in Section 2.1.2.

The horizontal distribution of the average number of assimilated observations per cycle in each experiment is shown in Figure 2. The larger number of assimilated observations over the center and east of the domain correspond to the ASWS observations. In this region we observed high values of precipitation during Nov 22 and is associated with the inflow of moisture by the South American low level jet. In Figure 3a the number of assimilated observations over
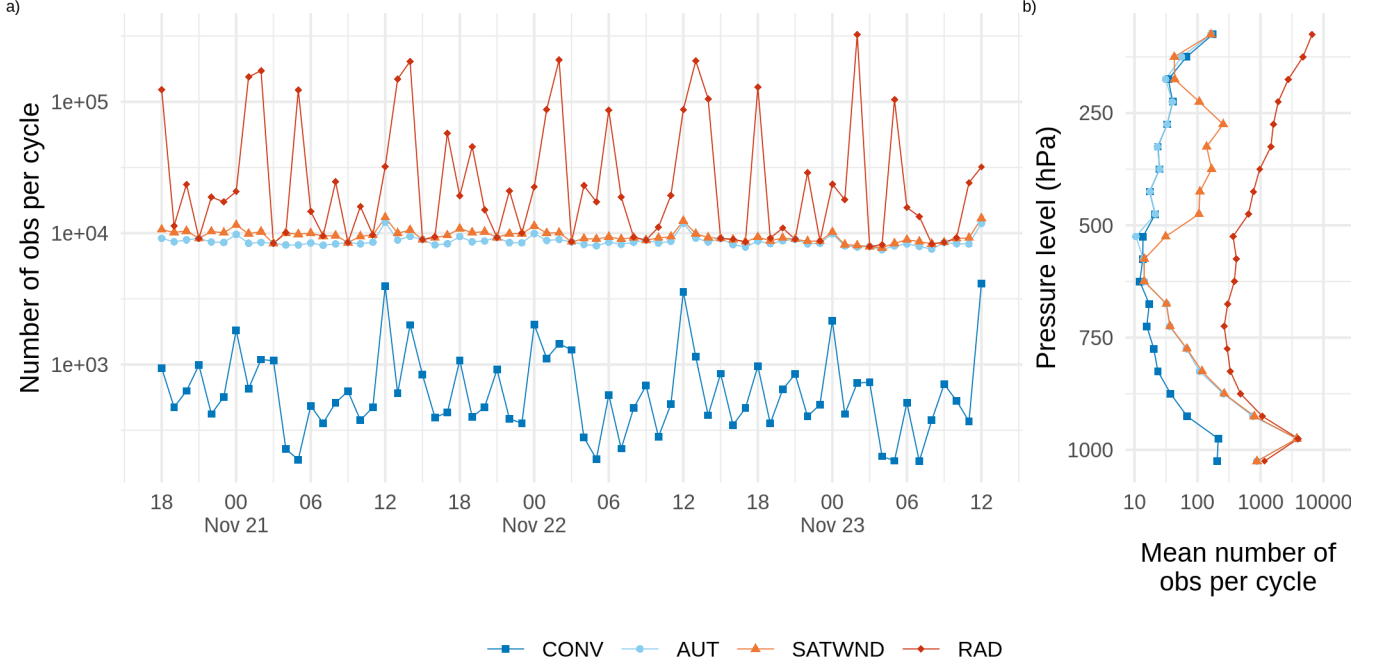
Figure 3: a) Number of available observations per cycle and b) time averaged number of observations per cycle and divided into 50 hPa-depth vertical layers for the CONV (blue squares and line), AUT (light blue dots and line), SATWND (orange triangles and line) and RAD (red diamond and line) experiments.

Table 3: Observation types assimilated in each experiment.

Obs type	CONV	AUT	SATWND	RAD
PREPBUFR	x	x	x	x
AUTSFC		x	x	x
SATWND			x	x
RAD				x

time is shown. Local maxima at 12 and 00 UTC found mainly in CONV is produced by the operational soundings. The strong variability in the number of radiance observations per cycle is also noticeable and depends on the satellite coverage. The maxima after 12 and 00 UTC correspond to the contribution of the multispectral sensors. The vertical distribution of the mean number of observations per cycle (Figure 3b shows a maximum in low levels due to the ASWS observations. Satellite-derived winds available in this particular case are maximum at the upper troposphere (between 500-250 hPa). Above 850 hPa, most of the observations correspond to radiance observations.

All the assimilation experiments start at 18 UTC Nov 20, 2018 and continue until 12 UTC Nov, 23 (totaling 67 hours/assimilation cycles). The initial ensemble is generated from a spin-up run without assimilating observations performed between 12 UTC and 18 UTC Nov 20 (Figure 4).
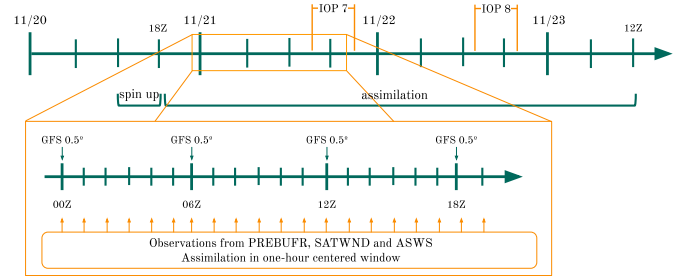

Figure 4: Diagram of the analysis cycles between Nov 20th, 18 UTC and Nov 23rd 12 UTC plus and spin up period of 6 hours. The zoomed section shows the assimilation for each hour that is performed within a one-hour centered window and new boundary conditions from GFS every 6 hours. Also the two Intensive Observation Periods (IOP) missions from the RELAMPAGO Field Campaign are shown.

2.3. Verification methods

A set of metrics are selected to evaluate different aspects of the analysis obtained in the experiments conducted in

6

this paper. These aspects include a validation of how uncertainty is quantified in the first-guess and in the analysis and how different experiments fit an independent set of observations which are not assimilated . To evaluate the consistency of the uncertainty quantification in the first-guess and in the analysis we use the Reduced Centered Random Variable (RCRV, Candille et al. (2007)) which is defined as:

$$RCRV = \frac{x_o - m}{\sqrt{\sigma_o^2 + \sigma^2}}$$

where x_o is the error σ_o, the mean m, and the standard deviation σ of the ensemble. The average of $RCRV$ computed over all the realizations represents the bias of the ensemble mean with respect to the observations normalized by the estimated uncertainty:

$$meanRCRV = E[RCRV]$$

The standard deviation of the $RCRV$ or $sdRCRV$ measures the agreement of the ensemble spread and the observational error with respect to the distance between the ensemble mean and the observations, and then the systematic over- or under- dispersion of the ensemble:

$$sdRCRV = \sqrt{\frac{M}{M-1}E[(RCRV - meanRCRV)^2]}$$

where M is the sample size. A reliable system will have no bias ($meanRCRV = 0$), and a standard deviation equal to 1, $sdRCRV = 1$. If the ensemble has a positive (negative) bias, $meanRCRV$ will be positive (negative). A $sdRCRV > 1$ ($sdRCRV < 1$), indicates that the ensemble is underdispersive (overdispersive).

The fit of the first-guess and analysis to a set of independent observations is computed based on the Root Mean Square Error (RMSE) and the BIAS:

$$RMSE = \sqrt{\frac{1}{N}\sum_{i=1}^{N}(X_i - O_i)^2}$$

$$BIAS = \frac{1}{N}\sum_{i=1}^{N}(X_i - O_i)$$

where O and X stand for independent observations and the analysis respectively.

For the comparison of the first-guess' precipitation with the precipitation estimates we compute a probabilistic Fraction Skill Score (FSS) for different sized sampling areas and thresholds, following Maldonado et al. (2021) and adaptations from Roberts (2008).

$$FSS = 1 - \frac{\frac{1}{N}\sum_{i=1}^{N}(P_{xi} - P_{oi})^2}{\frac{1}{N}\sum_{i=1}^{N}(P_{xi})^2 + \frac{1}{N}\sum_{i=1}^{N}(P_{oi})^2}$$

where P_x and is the probability of occurrence of accumulated rainfall over a specified threshold computed from

the ensemble and P_o is 1 when the observed accumulated precipitation is over the same threshold and 0 otherwise. This probabilistic formulation uses the information from the full ensemble thus avoiding the smoothing effect of the ensemble mean which can particularly affect localized extreme precipitation values. The FSS was applied to the accumulated precipitation over 6 hr periods by adding the 1-hr accumulated precipitation forecasts over 6 consecutive assimilation cycles.

3. Results

3.1. Ensemble reliability

To investigate the ability of the ensemble to represent the possible states of the atmosphere taking into account the uncertainties of the model and the observations we calculated the mean and sd of the first-guess RCRV for the RAD experiment between 18 UTC Nov, 20 and 12 UTC Nov, 23. As this experiment assimilates all types of observations used in this work, it is possible to analyse the reliability of the ensemble by comparing with each type of observation. Figure 5 shows the sd RCRV for surface observations computed and box-averaged to a 2.5° grid. The wind (Figure 5 a) has a $sdRCRV$ close to 1 suggesting a good agreement between the ensemble spread, the forecast error and the observation error. For the temperature (Figure 6 b and d), the results are similar except for some areas to the west of the domain where sd RCRV can be as high as 4.5. These areas were studied in detail and it was found that the mean innovation was overly large. The main reason for this is the complexity of the topography, usually associated with differences between the model topography and the station height leading to relatively large errors.

Figure 6 shows the mean and standard deviation of the RCRV for the upper-air observations. Figure 7 a and b show the RCRV statistics in soundings (ADPUPA) and aircraft (AIRCAR and AIRCFT). Both ADPUPA and AIRCFR show a general good agreement between the ensemble spread and the observation error while AIRCAR presents an irregular profile with values that suggests that the error for this type of observation is overestimated. ADPUPA and AIRCAR also present a mean RCRV profile near zero on middle and upper levels but ADPUPA shows a cold bias at low levels, a characteristic already studied in Ruiz 2010 and Dillon 2021.

For satellite-derived wind observations (Figure 7 c)) in low levels, the profiles of b and d that are not close to the expected values with a negative bias and an overestimation of the observation error. This characteristic persists throughout all levels. Wind estimation derived from water vapor channels shows a bias close to zero in upper levels.

The mean RCRV profiles calculated from the radiance observations (Figure 7 d)) shows almost no bias and the same happens if the mean RCRV is calculated over each channel of each sensor indicating that the bias correction algorithm worked as expected. The sd RCRV values are
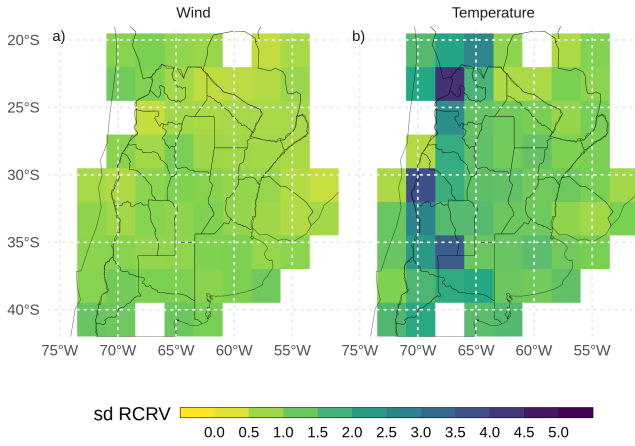
Figure 5: sd RCRV calculated for surface observations of a) wind, and b) temperature, averaged over 2.5º boxes.

less than 1 for all sensors possible due to an overestimation of the observation errors.

Overall these results indicate that the ensemble spread is consistent with the short-range forecast error and that systematic errors are relatively small for most of the observation types used in this work Moreover, these results suggest the inflation parameter $\beta = 0.9$ is adequate.

3.2. Impacts of assimilated observations

In this section we investigate the impact of assimilating different observation types on variables which are particularly relevant for the occurrence of deep moist convection. The analysis is performed over a smaller domain (red box in Figure 1) to avoid high topography effects and to focus on the region most directly affected by the MCS. Figure 8 a to c shows the difference between AUT and CONV in the spatially averaged vertical profile of temperature. The assimilation of ASWS observations results in a colder planetary boundary layer (PBL). This cooling effect has a clear diurnal cycle that is stronger during night time. (Figure 8 a). The impact of ASWS observations is not limited to the PBL, as significant impact in mid to upper levels is also found during the mature stage of the MCS. The warming in AUT present between 500 and 300 hPa is produced by the development of stronger convection in this experiment compared to CONV. SATWND observations have an almost negligible impact on the mean temperature (Figure 8 b)). The assimilation of radiances produces significant impacts in low level temperature. These observations produce a warming effect in the analyzed PBL which partially compensate for the cooling effect of ASWS observations, particularly during the first 24 hours. After that period the impact of assimilating radiances becomes smaller in the first levels. The impact of the radiances is

also important during the mature stage of the MCS and extended to the end of the simulation period.

Comparing the specific humidity in the experiments (Figure 8 d-f) the impact of assimilating ASWS with larger spatial and temporal resolution is most significant at low levels (Figure 8 d)). The PBL in the AUT experiment is consistently moister than in the CONV experiment. The increase in low-level moisture by a denser surface network is consistent with previously reported dry biases in the WRF model over the region [Ruiz 2010, algún otro del SMN?]. The impact of satellite-derived winds are smaller and only important after 18 UTC Nov, 21 at low levels. As for the temperature, the impact of RAD observations reduces the impact of ASWS at low levels until 12 UTC Nov, 22. Radiances also reduce low-middle level moisture above the boundary layer where the impact of surface observations is not so important. This effect is significant during the development of the MCS between 00 and 12 UTC Nov, 22.

The impacts on the wind components are shown in Figure 9. The shaded values correspond to the difference between the experiments while the contours represent the spatially averaged vertical wind profile for the experiment highlighted in bold on each figure. For example, Figure 9 a) shows the difference between AUT and CONV (shaded) and the averaged zonal wind for AUT as is the experiment with more assimilated observations on that panel.

The assimilation of ASWS produces an increase of zonal wind and a decrease of meridional wind at low levels during the first two days of analysis. Therefore, these observations generate a reduction of the northerly flow associated with the South American low level jet during night time. After 18 UTC Nov, 22 the opposite effect is observed when the MCS is moving through the domain. At upper levels, the sign of the impact varies throughout the experiment period becoming larger during the development of the MCS. During Nov 22 and 23 the impact of assimilating ASWS in AUT, produces an increase of northerly wind in upper levels. This could indicate a stronger development of convection and therefore an increase in the outflow of convective cells. The assimilation of satellite-derived winds produces impacts only in middle and upper levels. The impact in the northerly wind is an increase of 0.8 m/s on average.

The assimilation of radiance observations produced a reduction in the westerly wind compared with SATWIND in low and upper levels. For the meridional wind, these observations produce an enhancement of the northerly low-level flow of $1 ms^{-1}$ on average, opposite to what is generated by the assimilation of ASWS observations. On upper levels and during Nov 22 and 23 the impact of assimilating radiances have the opposite effect on the meridional wind when compared with the impact of the ASWS observations.

To summarize these results, ASWS observations that have high spatial and temporal resolution produce major impacts throughout the troposphere and mainly at low levels. These changes in the planetary boundary layer can substantially affect the development of the convection. On
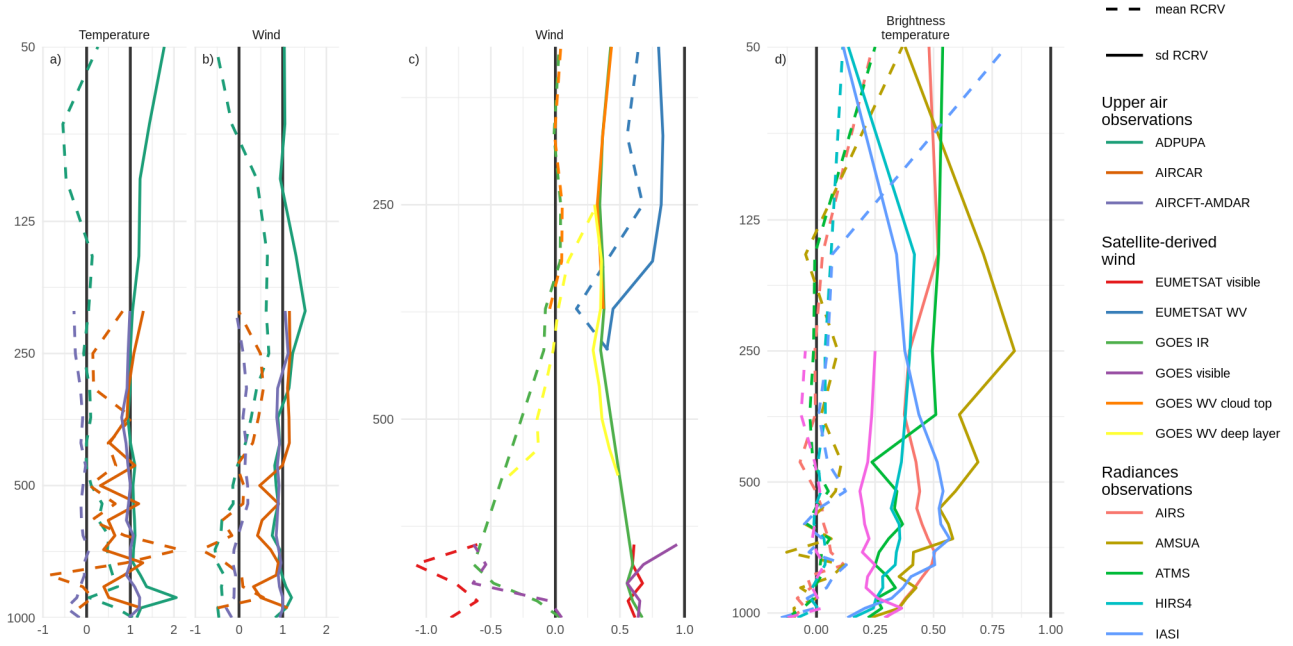
Figure 6: Vertical profiles of mean RCRV and sd RCRV for a) and b) sounding and aircraft observations, c) satellite-derived winds, and d) brightness temperature observations.

the other hand, radiances also produce important impacts but these are, in general, opposite to those of ASWS observatios. Spatial fields of different variables at 00 UTC Nov, 22 will be analyzed next to obtain an overview of the environment prior to the development of the MSC.

To investigate how changes in the PBL can modify the pre-convective environment we compare the horizontal distribution of the northerly flow, precipitable water, low level temperature and CAPE for the analysis at 00 UTC Nov, 22. At that moment the first convection cells were developing on the southern region of the domain along the cold front. Figure 10 a) shows the precipitable water (shaded) and the vertically averaged low-level meridional wind component (contours). We found that the moist tongue extending over Northern and central Argentina is enhanced by the assimilation of denser surface observations. The moisture increase is particularly stronger at the southern tip of this tongue at the boundary of the relatively colder air mass where the convection leading to the MCS was triggered. As a result AUT and SATWND experiments are very similar, with values of precipitable water over 55 kg/m2 north of 30°S and a similar vertical distribution of specific humidity (not shown). RAD has lower precipitable water content than previous experiments but not as low as CONV. The distribution of moisture at low and medium levels observed in RAD can be explained by a combination of the drying that generates the assimilation of radiances and a higher moisture transport due to the stronger northerly wind with values above 10 m/s over the centre of the domain.

The potential temperature on the PBL (Figure 11 b) resembles the characteristics observed on the temperature

profiles in Figure 8 a and c. On average the PBL in AUT and SATWND is colder than in CONV while RAD shows a warmer PBL due to the assimilation of radiance observations. Figure 11 c) shows the most unstable convective available potential energy (MCAPE, shaded) and the 0 to 6 km wind shear. The values of MCAPE in CONV do not exceed 2000 JKg-1 while the rest of the experiments show maximum MCAPE over 4000 JKg-1. The decrease of the specific humidity in lower levels present in RAD could explain the slightly lower values of MCAPE that is partially compensated by an increase in the temperature in the PBL, compared with AUT or SATWND. The wind shear is more intense in RAD reaching values over 15 ms-1 over the area of maximum MCAPE at the southern tip of the northerly low-level flow. Stronger wind shear between 0 and 6 km has been associated with the development of more intense and organized MCS [Chen 2015,] and also with conditions favorable for supercells (e.g. Markowsky and Richardson 2010). Particularly in this case we can see that on the Southern tip of the strong CAPE region, the 0-6 km wind shear is over 15 ms-1 which is considered favorable for supercell occurrence, while in the CONV experiment the intersection of the unstable warm air and the high shear is slightly smaller and occurs at lower MCAPE values.

3.3. Verification

Analysis verifications are performed to assess the skill of each experiment to represent the atmospheric circulation, particularly associated with the MSC development and precipitation. Figure 12 shows the first-guess hourly accu-

mulated precipitation averaged over a longitud range between 67°W and 54.5°W as a function of time and latitude in the different experiments, and estimated precipitation by IMERG. The heaviest precipitation (over 12 mm/h) starts during the afternoon of Nov 22 and continues during Nov 23 after the end of the experiments. In all the experiments, the accumulated precipitation in the short-range forecasts underestimate the precipitation. This is particularly evident on CONV where the convection initiation is significantly delayed with respect to the observations and occurs further north with respect to the observed initiation. AUT, SATWND and RAD better capture the timing and location of convective initiation. On RAD the initiation is delayed respecto to AUT and SATWND possibly related to the lower content of precipitable water and MCAPE on the southern tip of the moist tongue. After 18 UTC Nov, 22 RAD shows improvements in precipitation rate and its distribution compared to the other experiments due to the enhanced development of the conveccion.

To quantify the spatial match between the estimated precipitation and the short range forecasted precipitation for the different experiments, we compute the FSS in 6-hours moving windows for different thresholds and spatial scales (Figure 13). All experiments show low values of FSS before and during the initiation of the MCS around 03 UTC Nov, 22, afterwards FSS values improve during the mature and dissipation stages of the MCS. The FSS for CONV is the lowest compared to the rest of the experiments and the differences are larger during the maturity and dissipation stages of the MCS. AUT and SATWND show similar FSSs indicating that satellite-derived winds assimilation has little impact on the precipitation for the present case study. The assimilation of radiance observations improves the skill of the 1-hour forecasted precipitation as the FSS in RAD is higher, particularly for the 25 mm threshold during the period of heaviest precipitation on Nov, 22. The enhancement is particularly important at the developing stage of the MCS (between 00 and 12 UTC Nov, 22 and for spatial scales above 500 km, not shown).

To complement the analysis of the representation of the MCS evolution by the different experiments, Figure 14 shows the maximum reflectivity in the column (COLMAX) for the CONV and RAD experiments ensemble mean at different times between 10 and 19 UTC Nov, 22th along with the observed reflectivity. These experiments were chosen because they represent the analysis with minimum and maximum number of assimilated observations. In addition, these experiments are the worst and best performing experiments with respect to precipitation. Overall none of the short range forecasts is able to capture the mesoscale details in the precipitation distribution. This is partially expected considering the relatively low horizontal resolution (10 km) which is not enough to appropriately capture the strength of the convective band associated with the MCS. Also, the ensemble mean produces a smoothing effect that reduces the amplitude of local maxima in the forecasted reflectivity field. RAD better represents the observed features of the

MSC showing an organized pattern over the centre domain at 10 and 13 UTC. The convection cells that initiate after 16 UTC in the northeast region are also present in the 1-hr forecast. CONV also captures the location of the MCS, but the convection seems to be less organised and much weaker than in RAD. Before and after the times shown in Figure 14, the agreement between experiment and observations is quite high in the regions where radar data are available.

Individual radiosondes were also compared with the experiments to analyse the specific characteristics of the atmosphere before and after the development of the MCS.

Figure 15 shows the RMSE and bias calculated by comparing the experiments with radiosonde data from the RELAMPAGO IOP07 from 15 to 21 UTC Nov, 21 (including 30 radiosondes) and IOP08 from 14 to 20 UTC Nov 22 (including 22 radiosondes). During the first period, no significant meteorological events were observed on the domain of interest, thus the synoptic situation corresponds to a warm day with an important humidity transport from the centre of South America. For the temperature, CONV presents a warm bias on the PBL of 1°C and an RMSE between 1 and 2.5°C that are slightly reduced by the assimilation of ASWS and radiances. The RMSE for temperature remains between 0.5 and 2°C throughout the profile and the assimilation has almost no effect in middle and upper levels. The dew point temperature shows a small dry bias in low levels that is corrected on AUT and SATWND. On middle levels (below 10 km) the bias is large and positive (8 - 10°C), indicating a more moist atmosphere in the analysis. The RMSE also grows with height where small variations of humidity produces major chances in dew point temperatures. The zonal wind has a significant positive bias around 10 km of 10 m/s, this means that all experiments present a stronger westerly wind that is in part corrected by the assimilation of radiance observations. Finally, the meridional wind shows small values of bias and RMSE through the vertical profile but the assimilation of radiance observations increases the northerly wind near the surface.

For the second period, corresponding to IOP08, none of the radiosondes was directly affected by the convective processes since the MSC crossed RELAMPAGO's region of study before the beginning of the observation period. Below 5km all experiments show a warm bias which decreases with the assimilation of ASWS and radiances. Between 5 and 12 km, the bias is cold and only the ASWS observations improves the analysis. The RMSE for AUT, SATWND and RAD remains below 2°C for almost all levels with small improvement in upper levels where radiance observations have the most impact. In terms of the dew point temperature, the analyses have a moist bias near the surface that increases with the incorporation of new observations. The moist bias in conjunction with the underestimation of the precipitation might be indicating that the convection processes on the model are not converting the available moisture into precipitation or that the model fails to represent boundary layer processes correctly. SATWND

presents the lowest RMSE overall while AUT and RAD are comparable between 4 and 12 km with values that do not exceed 7°C. Once again, the zonal wind is overestimated on the analyses with a positive bias on middle and upper layers. For this period only RAD shows an improvement on the upper layers of the troposphere. In low levels the meridional wind presents a positive bias, indicating an underestimation of the northerly wind principally in AUT, SATWND and RAD. In middle levels both AUT and SATWND have almost no bias while RAD shows a positive bias of 2.5 m/s while its RMSE does not exceed 5 m/s.

To summarize, the results suggest that the assimilation of observations with high temporal and spatial frequency generate an important impact on the PBL, primarily on the precipitable water content, that leads to the development of deep convection and heavy precipitation closer to the observed case study. While the assimilation of satellite-derived wind does not impact substantially on the analysis, this is possible due to the small number of observations in low levels. The assimilation of radiance observations produces a better development of the convection mainly during the mature state of the CSM leading to an increase in the accumulated precipitation.

4. Conclusions

References

Bao, Y., Xu, J., Powell Jr., A.M., Shao, M., Min, J., Pan, Y., 2015. Impacts of AMSU-A, MHS and IASI data assimilation on temperature and humidity forecasts with GSI–WRF over the western United States. Atmos. Meas. Tech. 8, 4231–4242. doi:10.5194/amt-8-4231-2015

Brooks, H.E., Lee, J.W., Craven, J.P., 2003. The spatial distribution of severe thunderstorm and tornado environments from global reanalysis data. Atmospheric Research 67-68, 73–94. doi:10.1016/S0169-8095(03)00045-0

Candille, G., Côté, C., Houtekamer, P.L., Pellerin, G., 2007. Verification of an Ensemble Prediction System against Observations. Mon. Wea. Rev. 135, 2688–2699. doi:10.1175/MWR3414.1

Cecil, D.J., Blankenship, C.B., 2012. Toward a Global Climatology of Severe Hailstorms as Estimated by Satellite Passive Microwave Imagers. Journal of Climate 25, 687–703. doi:10.1175/JCLI-D-11-00130.1

Chen, F., Dudhia, J., 2001. Coupling an Advanced Land Surface–Hydrology Model with the Penn State–NCAR MM5 Modeling System. Part I: Model Implementation and Sensitivity. Monthly Weather Review 129, 569–585. doi:10.1175/1520-0493(2001)129<0569:CAALSH>2.0.CO;2

de Elía, R., Vidal, L., Lohigorry, P., 2017. El SMN y la red argentina de radares meteorológicos [WWW Document]. URL http://hdl.handle.net/20.500.12160/625

Dillon, M.E., García Skabar, Y., Kalnay, E., Ruiz, J.J., Collini, E.A., 2019. Sensibilidad de un sistema de asimilación de datos por ensambles a diferentes configuraciones, implementado en el sur de Sudamérica. Meteorológica 44, 15–34.

Dillon, M.E., Maldonado, P., Corrales, P., García Skabar, Y., Ruiz, J.J., Sacco, M., Cutraro, F., Mingari, L., Matsudo, C., Vidal, L., Rugna, M., Hobouchian, M.P., Salio, P., Nesbitt, S., Saulo, C., Kalnay, E., Miyoshi, T., n.d. A Rapid Refresh ensemble based Data Assimilation and Forecast system for the RELAMPAGO field campaign. Atmospheric Research.

Dillon, M.E., Skabar, Y.G., Ruiz, J., Kalnay, E., Collini, E.A., Echevarría, P., Saucedo, M., Miyoshi, T., Kunii, M., 2016. Application of the WRF-LETKF Data Assimilation System over Southern South America: Sensitivity to Model Physics. Wea. Forecasting 31, 217–236. doi:10.1175/WAF-D-14-00157.1

Earth Observing Laboratory, U. -, 2020. Multi-network composite highest resolution radiosonde data. Version 1.3. UCAR/NCAR - earth observing laboratory.

Gao, F., Huang, X.-Y., Jacobs, N.A., Wang, H., 2015. Assimilation of wind speed and direction observations: Results from real observation experiments. Tellus A: Dynamic Meteorology and Oceanography 67, 27132. doi:10.3402/tellusa.v67.27132

Garcia, F., Ruiz, J., Salio, P., Bechis, H., Nesbitt, S., 2019. Argentina mesonet data. Version 1.1. UCAR/NCAR - earth observing laboratory.

Grell, G.A., Freitas, S.R., 2013. A scale and aerosol aware stochastic convective parameterization for weather and air quality modeling. Atmos. Chem. Phys. Discuss. 13, 23845–23893. doi:10.5194/acpd-13-23845-2013

gustavo Goncalves de Goncalves, L., Sapucci, L., Vendrasco, E., de Mattos, J.G., Ferreira, C., Khamis, E., Cruz, N., 2015. A rapid update data assimilation cycle over South America using 3DVar and EnKF, in: The 20th International TOVS Study Conference (ITSC-20). The 20th International TOVS Study Conference (ITSC-20), Lake Geneva, Wisconsin, USA.

Ha, S.-Y., Snyder, C., 2014. Influence of Surface Observations in Mesoscale Data Assimilation Using an Ensemble Kalman Filter. Monthly Weather Review 142, 1489–1508. doi:10.1175/MWR-D-13-00108.1

Han, Y., Van Delst, P., Liu, Q., Weng, F., Yan, B., Treadon, R., Derber, J., 2006. JCSDA Community Radiative Transfer Model (CRTM)—version 1, NOAA Technical Report NESDIS 122. Washington, D.C.

Hong, S.-Y., Kim, J.-H., Lim, J.-o., Dudhia, J., 2006. The WRF Single Moment 6-Class Microphysics Scheme (WSM6). Journal of the Korean Meteorological Society 42, 129–151.

Hong, S.-Y., Noh, Y., Dudhia, J., 2006. A New Vertical Diffusion Package with an Explicit Treatment of Entrainment Processes. Mon. Wea. Rev. 134, 2318–2341. doi:10.1175/MWR3199.1

Hu, M., Ge, G., Zhou, C., Stark, D., Shao, H., Newman, K., Beck, J., Zhang, X., 2018. Grid-point Statistical Interpolation (GSI) User's Guide Version 3.7. Developmental Testbed Center.

Huffman, G., Bolvin, D., Braithwaite, D., Hsu, K., Joyce, R., Kidd, C., Nelkin, E., Sorooshian, S., Tan, J., Xie, P., 2018. NASA Global Precipitation Measurement (GPM) Integrated Multi-satellitE Retrievals for GPM (IMERG). National Aeronautics and Space Administration (NASA).

Hunt, B.R., Kostelich, E.J., Szunyogh, I., 2007. Efficient data assimilation for spatiotemporal chaos: A local ensemble transform Kalman filter. Physica D: Nonlinear Phenomena 230, 112–126. doi:10.1016/j.physd.2006.11.008

Iacono, M.J., Delamere, J.S., Mlawer, E.J., Shephard, M.W., Clough, S.A., Collins, W.D., 2008. Radiative forcing by long-lived greenhouse gases: Calculations with the AER radiative transfer models. J. Geophys. Res. 113, D13103. doi:10.1029/2008JD009944

Janjić, Z.I., 1994. The Step-Mountain Eta Coordinate Model: Further Developments of the Convection, Viscous Sublayer, and Turbulence Closure Schemes. Mon. Wea. Rev. 122, 927–945. doi:10.1175/1520-0493(1994)122<0927:TSMECM>2.0.CO;2

Jones, T.A., Otkin, J.A., Stensrud, D.J., Knopfmeier, K., 2013. Assimilation of Satellite Infrared Radiances and Doppler Radar Observations during a Cool Season Observing System Simulation Experiment. Mon. Wea. Rev. 141, 3273–3299. doi:10.1175/MWR-D-12-00267.1

Kain, J.S., 2004. The Kain–Fritsch Convective Parameterization: An Update. JOURNAL OF APPLIED METEOROLOGY 43, 12.

Lin, H., Weygandt, S.S., Benjamin, S.G., Hu, M., 2017. Satellite Radiance Data Assimilation within the Hourly Updated Rapid Refresh. Wea. Forecasting 32, 1273–1287. doi:10.1175/WAF-D-16-0215.1

Maldonado, P., Ruiz, J., Saulo, C., 2021. Sensitivity to Initial and Boundary Perturbations in Convective-Scale Ensemble-Based Data Assimilation: Imperfect-Model OSSEs. SOLA 17, 96–102. doi:10.2151/sola.2021-015

Matsudo, C., García Skabar, Y., Ruiz, J., Vidal, L., Salio, P., 2015. Verification of WRF-ARW convective-resolving forecasts over Southeastern South America. Mausam 66, 445–456.

Miyoshi, T., Kunii, M., 2012. Using AIRS retrievals in the WRF-LETKF system to improve regional numerical weather prediction. Tellus A: Dynamic Meteorology and Oceanography 64, 18408. doi:10.3402/tellusa.v64i0.18408

Nakanishi, M., Niino, H., 2009. Development of an Improved Turbulence Closure Model for the Atmospheric Boundary Layer. JMSJ 87, 895–912. doi:10.2151/jmsj.87.895

Necker, T., Geiss, S., Weissmann, M., Ruiz, J., Miyoshi, T., Lien, G., 2020. A convective-scale 1,000-member ensemble simulation and potential applications. Q.J.R. Meteorol. Soc 146, 1423–1442. doi:10.1002/qj.3744

Nesbitt, S.W., Salio, P.V., Ávila, E., Bitzer, P., Carey, L., Chandrasekar, V., Deierling, W., Dominguez, F., Dillon, M.E., Garcia, C.M., Gochis, D., Goodman, S., Hence, D.A., Kosiba, K.A., Kumjian, M.R., Lang, T., Luna, L.M., Marquis, J., Marshall, R., McMurdie, L.A., Nascimento, E.L., Rasmussen, K.L., Roberts, R., Rowe, A.K., Ruiz, J.J., Sabbas, E.F.M.T.S., Saulo, A.C., Schumacher, R.S., Skabar, Y.G., Machado, L.A.T., Trapp, R.J., Varble, A., Wilson, J., Wurman, J., Zipser, E.J., Arias, I., Bechis, H., Grover, M.A., 2021. A storm safari in Subtropical South America: Proyecto RELAMPAGO. Bulletin of the American Meteorological Society -1, 1–64. doi:10.1175/BAMS-D-20-0029.1

Ouaraini, R.E., Berre, L., Fischer, C., Sayouty, E.H., 2015. Sensitivity of regional ensemble data assimilation spread to perturbations of lateral boundary conditions. Tellus A: Dynamic Meteorology and Oceanography 67, 28502. doi:10.3402/tellusa.v67.28502

Rasmussen, K.L., Zuluaga, M.D., Houze, R.A., 2014. Severe convection and lightning in subtropical South America. Geophysical Research Letters 41, 7359–7366. doi:10.1002/2014GL061767

Roberts, N., 2008. Assessing the spatial and temporal variation in the skill of precipitation forecasts from an NWP model. Meteorological Applications 15, 163–169. doi:10.1002/met.57

Singh, R., Ojha, S.P., Kishtawal, C.M., Pal, P.K., Kiran Kumar, A.S., 2016. Impact of the assimilation of INSAT-3D radiances on short-range weather forecasts: Assimilation of INSAT-3D Radiances. Q.J.R. Meteorol. Soc. 142, 120–131. doi:10.1002/qj.2636

Skamarock, W.C., Klemp, J.B., Dudhia, J., Gill, D.O., Barker, D.M., Duda, M.G., Huang, X.-Y., Wang, W., Powers, J.G., 2018. A Description of the Advanced Research WRF Version 3.

Sun, J., Xue, M., Wilson, J.W., Zawadzki, I., Ballard, S.P., Onvlee-Hooimeyer, J., Joe, P., Barker, D.M., Li, P.-W., Golding, B., Xu, M., Pinto, J., 2014. Use of NWP for Nowcasting Convective Precipitation: Recent Progress and Challenges. Bulletin of the American Meteorological Society 95, 409–426. doi:10.1175/BAMS-D-11-00263.1

Weston, P., Geer, A., Bormann, N., Bormann, N., 2019. Investigations into the assimilation of AMSU-A in the presence of cloud and precipitation [WWW Document]. EUMETSAT/ECMWF Fellowship Programme Research Report. doi:10.21957/ewahn9ce

Whitaker, J.S., Hamill, T.M., 2012. Evaluating Methods to Account for System Errors in Ensemble Data Assimilation. Mon. Wea. Rev. 140, 3078–3089. doi:10.1175/MWR-D-11-00276.1

Zhu, K., Xue, M., Pan, Y., Hu, M., Benjamin, S.G., Weygandt, S.S., Lin, H., 2019. The Impact of Satellite Radiance Data Assimilation within a Frequently Updated Regional Forecast System Using a GSI-based Ensemble Kalman Filter. Adv. Atmos. Sci. 36, 1308–1326. doi:10.1007/s00376-019-9011-3

Zhu, Y., Derber, J., Collard, A., Dee, D., Treadon, R., Gayno, G., Jung, J.A., 2014. Enhanced radiance bias correction in the National Centers for Environmental Prediction's Gridpoint Statistical Interpolation data assimilation system. Quarterly Journal of the Royal Meteorological Society 140, 1479–1492. doi:10.1002/qj.2233

Zhu, Y., Liu, E., Mahajan, R., Thomas, C., Groff, D., Van Delst, P., Collard, A., Kleist, D., Treadon, R., Derber,

J.C., 2016. All-Sky Microwave Radiance Assimilation in NCEP's GSI Analysis System. Mon. Wea. Rev. 144, 4709–4735. doi:10.1175/MWR-D-15-0445.1